

Effect of Heating Rate on the Pressureless Sintering Densification of a Nickel-Based Superalloy



DAVID LEVASSEUR and MATHIEU BROCHU

Pressureless sintering of Inconel 718 has important technological applications for the densification of metal injection molding or additive manufacturing of parts with powder/binder systems. The effect of heating rates ranging from 15 to 200 K/minute on the sintering behavior of fine (–325 mesh) Inconel 718 powders was studied using the master sintering curve (MSC) concept. A pressureless pulsed electric current sintering setup was used to heat samples. The temperature at the onset of sintering increased as the heating rate increased. The formation of a supersolidus liquid fraction was shifted toward higher temperatures for increased heating rates. The apparent activation energy of sintering was obtained by least squares fitting of the sintering data to the MSC and was in good agreement with the lattice diffusion activation energy of the alloying elements present in Inconel 718. The MSC followed different kinetics for low heating rates (≤ 50 K/minute) and high heating rates (≥ 75 K/minute), and these differences were related to liquation kinetics.

DOI: 10.1007/s11661-016-3361-6

© The Minerals, Metals & Materials Society and ASM International 2016

I. INTRODUCTION

INCONEL 718 is a nickel-based superalloy that is widely used in hot zones of land-based turbines as well as in jet engines.^[1] Among the existing manufacturing routes for this alloy, powder metallurgy (PM) is advantageous as it yields a low buy-to-fly ratio for complex-shaped parts. Unfortunately, Inconel 718 is hard to sinter to full density owing to its high strength at high temperatures; accordingly, it requires high sintering temperatures and pressure-assisted processes.^[2] Metal injection molding (MIM) with Inconel 718 is used to produce green parts^[3] that can be sintered to densities exceeding 97 pct. Full density is achieved after a hot isostatic pressing treatment.^[4–7] Based on previous studies on the sintering of MIM Inconel 718, the powder particle size varies from a D_{50} of 10 to 22 μm , and sintering temperatures vary between 1533 K and 1573 K (1260 °C and 1300 °C), with a holding time of 1 to 6 hours.^[3–8] The reported mechanical properties of the sintered, hot isostatic pressed, and aged parts are summarized in Table I.

The reduced strength and elongation of Inconel 718 PM parts compared to cast or wrought parts can be explained by their lower density and the presence of brittle second phases, such as Laves phase and MC carbides that form during sintering.^[6] Özgün *et al.*^[6] have studied the effect of microstructure on mechanical

properties of sintered Inconel 718 MIM parts. They highlighted the unusually high volume fraction of MC carbides that form due to carbon pickup from the binder used to produce MIM green parts. The formation of MC carbides is associated with scavenging of the second-phase forming elements, such as Ti and Nb, which precipitate as γ' ($\text{Ni}_3(\text{Al,Ti})$) and γ'' (Ni_3Nb) and confer beneficial mechanical properties at high temperatures [up to 923 K (650 °C)]. As depicted in the mechanical properties shown in Table I, the production of Inconel 718 MIM parts with mechanical properties close to those of wrought parts necessitates hot isostatic pressing post-treatment. The achievement of full density directly after sintering would improve the properties of sintered materials. Advanced sintering technology such as induction sintering and spark plasma sintering are high heating rate techniques and have been shown to sinter nickel metal powders to high density in very short time.^[8,9] In this study, a wide range of heating rates were used to study the densification and microstructure evolution of Inconel 718 sintered parts based on the master sintering curve concept to assess the optimal sintering conditions for the direct production of Inconel 718 PM parts.

A. Master Sintering Curve

The master sintering curve (MSC) concept is a useful framework to predict pressureless sintering behavior from experimental densification data.^[15] The MSC analysis was developed by Su and Johnson to model the pressureless sintering behavior of metals and ceramics using the apparent activation energy from a few dilatometer densification tests performed at different heating rates. Considering that only a single dominant diffusion mechanism is active during sintering, Eq. [1]

DAVID LEVASSEUR, R&D Project Manager, is with the Quebec Metallurgy Center, Cegep de Trois-Rivières, 3095 Westinghouse Street, Trois-Rivières G9A 5E1, Canada. MATHIEU BROCHU, Associate Professor, is with the Mining and Materials Engineering Department, McGill University, 3610 University Street, Montreal H3A 0C5, Canada. Contact e-mail: Mathieu.brochu@mcgill.ca

Manuscript submitted August 11, 2015.

Article published online February 8, 2016

Table I. Summary of Published Data on the Sintering of Inconel 718 MIM Parts

Authors	Process	Density (g/cm ³)/(Pct TD)	YS (MPa)	UTS (MPa)	EL (Pct)	Grain Size (μm)	References
Mechanical Properties of Sintered Inconel 718 at Room Temperature							
Wohlfromm <i>et al.</i>	MIM + HT	7.99 (97.2 pct)	840	1259	21	NA	5
	MIM + HIP + HT	8.19 (99.6 pct)	908	1340	23	NA	5
Valencia <i>et al.</i>	MIM	8.2 (98.7 pct)	NA	NA	NA	28	4
	MIM + HT	8.21 (98.9 pct)	1062	1238	11.4	NA	4
	MIM + HIP	8.26 (99.5 pct)	1133	1350	14.2	25.6	4
Davies <i>et al.</i>	MIM	NA	503	936	20	<15	10
	MIM + HT	NA	1046	1211	6	<15	10
Schmees <i>et al.</i>	MIM + HIP + HT	NA	1139	1350	14.1	NA	11
Youhua <i>et al.</i>	MIM	98 pct	876	1054	25.4	NA	12
	MIM + HT	98 pct	1124	1304	8.7	NA	12
	MIM + HIP	100 pct	824	1009	39.3	NA	12
	MIM + HIP + HT	99.90 pct	1078	1250	21.7	NA	12
Özgün <i>et al.</i>	MIM	97.30 pct	506	667	5.8	20–30	6
	MIM + HT	97.30 pct	780	1022	5.3	NA	6
	Cast	8.22	915	1090	11		13
	Wrought	8.22	1185	1435	21		13
	AMS 5662M-2009 Min Requirements		1034	1241	12		14

can be used to predict changes in density over time during sintering:

$$\frac{d\rho}{3\rho dt} = \frac{\gamma\Omega(\Gamma(\rho))D_0}{kT(G[\rho])^n} \exp\left(\frac{Q}{RT}\right), \quad [1]$$

where ρ is the relative density, t is time, γ is the surface energy, Ω is the atomic volume, Γ is the lumped scaling parameter as described by Hansen *et al.*,^[16] D_0 is the appropriate diffusion constant (grain boundary or lattice diffusion), k is the Boltzmann constant, T is temperature, G is grain size, $n = 3$ for lattice diffusion and 4 for grain boundary diffusion, R is the gas constant, and Q is the apparent activation energy of sintering. If the lumped scaling parameter and grain size are functions of density alone, then Eq. [1] can be reorganized and integrated as follows:

$$\frac{k}{\Omega D_0} \int_{\rho_0}^{\rho} \frac{(G(\rho))^n}{3\rho\Gamma(\rho)} d\rho = \int_0^t \frac{1}{T} \exp\left(-\frac{Q}{RT}\right) dt, \quad [2]$$

where ρ_0 represents the green density. The terms in Eq. [2] can be arranged to separate the material properties on the left-hand side from Q and the temperature–time data on the right-hand side as follows:

$$\Phi(\rho) = \Theta(t, T(t)), \quad [3]$$

where $\Phi(\rho)$ includes all the material-related parameters except for Q , and $\Theta(t, T(t))$ is the “thermal work” term, which can be integrated by numerical methods from the temperature profiles of different sintering tests or from dilatometer curves. The activation energy Q can be evaluated from the densification curves by two methods.^[17,18] One is to perform a least square fit algorithm (minimum sum of squared residual between model and data) of the densification data as a function of the thermal work computed at different activation energies.^[17,19] Another route to extract the activation

energy from the experimental data is based on the following relation:^[18,20]

$$\ln\left(T \frac{dT d\rho}{dt dT}\right) = -\frac{Q}{RT} + \ln[f(\rho)] + \ln A - n \ln dG, \quad [4]$$

where $f(\rho)$ is a function of density and A is a material parameter. Mathematical manipulations allows Eq. [4] to take on the form of $y = mx + b$, where Q can be determined at a specific sintered density from the Arrhenius plot of $\ln(T dT/dt d\rho/dT)$ vs $1/T$ for each heating rate densification curves. This method assumes the grain size is only dependant on density. The activation energy is found from the slope (m) of the linear fit for each heating rate dataset $Q = -mR$. Once the apparent activation energy of sintering is determined empirically, a single function can be used to predict the density as a function of thermal work.

However, a drawback of the MSC model is that it considers only a single sintering mechanism responsible for shrinkage. The activation energy of this mechanism is related to the activation energy for diffusion, which is usually proportional to the amount of grain boundary diffusion and lattice diffusion that occurs within the system. A shift in sintering mechanism can then be readily observed, as it would change the MSC parameter and apparent activation energy. The development of an MSC analysis would permit postulations regarding the effectiveness of high heating rate sintering cycles for the processing of Inconel 718 PM parts.

II. EXPERIMENTAL METHOD

The prealloyed gas-atomized powder feedstock (low oxygen content and spherical morphology) used in this study was AMDRY 1718 supplied by Oerlikon (formerly Sulzer Metco; Winterthur, Switzerland). The

chemical composition of the powder, as provided by the supplier, is presented in Table II.

The powder size distribution was characterized by a laser interferometer; the geometric mean particle size was 33 μm , and geometric standard deviation was 8 μm .

The compacts were prepared by slip casting based on a procedure developed by Hamjrle and Anger.^[21] Following this procedure, they obtained carbon contamination ranging from 100 to 300 ppm.^[22] The powder was mixed with a solution of ammonium alginate, slip cast, and dried for at least 24 hours. The slip cast compacts were cut into cubes of 5 \times 5 \times 5 mm. The binder was removed from the green compacts in a vacuum furnace (2×10^{-4} torr) at 788 K (515 $^{\circ}\text{C}$) for 30 minutes and then furnace cooled. Assuming a theoretical density (TD) of Inconel 718 of 8.22 g/cm³, the initial density of the binder-less compacts was 61 \pm 3 pct TD based on the Archimedes method. The compacts were then sintered in the pulsed electric current sintering equipment with a custom pressureless die assembly inspired by Bradbury and Olevsky,^[23] as shown in Figure 1.

The sample was set in an open alumina crucible in the graphite die assembly and sintered in a Thermal Technologies 10-3 SPS press. The control thermocouple was set in the lower punch 2 mm below the sample chamber. The pressure applied to the die assembly was 5 MPa to ensure good electrical contact, which was only sustained by the graphite insert forming the sample chamber. The true temperature of the sample was corrected for each heating rate by calibrating the process temperature against the melting temperature of pure copper and pure nickel for various heating rates. It is assumed for modeling purpose that the heating rate of the sample inside the crucible is the same as the heating rate measured by the thermocouple in the lower punch.

The sintering of the binder-less compacts was performed at heating rates of 15, 25, 50, 75, 100, and 200 K/minute. Interrupted tests were used to build a density–temperature curve for each heating rate to mimic a dilatometer trace. At the tested temperature, the power was turned off and the sample was cooled to room temperature within 10 minutes, with an initial cooling rate of approximately 300 K/minute. Within 1 minute, the temperature dropped to below 70 pct of the T_m of Inconel 718, at which point sintering is negligible. The sample density was measured by the Archimedes method. Metallographic analysis was performed by cutting with a low-cutting speed wafering blade, cold mounting, and impregnation in epoxy before grinding with 600 grit SiC paper and polishing with 9, 1 μm diamond suspension, and colloidal silica solutions on appropriate cloths. Grain size was evaluated by an image analysis (Buehler OmniMet, Lake Bluff, IL, USA) of light optical micrographs (Nikon Eclipse LV150;

Tokyo, Japan) for samples etched with a solution consisting of 10 mL of HNO₃, 5 mL of glacial acetic acid, and 85 mL of H₂O under 1.5 V for 8 seconds. The porosity measurements were performed by image analysis with Clemex software (Longueuil, Canada) for images obtained using a light optical microscope (Olympus, Tokyo, Japan) at 50 times magnification using a mosaic picture of cross-sections of a polished sample.

III. RESULTS

A. Densification Experiments

The densification plots for all sintering experiments are shown in Figure 2. The sintering densification curves for all sets of experimental data followed a classical sigmoidal shape and were thus fitted to a sigmoidal curve using Eq. [5]. The densification curves are shifted toward higher temperatures as the heating rate increases; however, there is a change of trend between the 50 and 75 K/minute curves.

As shown in Figure 3, the second derivative of the sigmoidal curve was computed to determine the onset temperature for densification for each heating rate. As expected, the densification onset temperature increased as the heating rate increased, but a discontinuity (*i.e.*, a dip) in the curve was observed for heating rates of 75 and 100 K/minute. The observed dip in densification onset temperature could indicate a change in sintering mechanism that could be visualized through the MSC analysis. Hereafter, two densification regimes will be

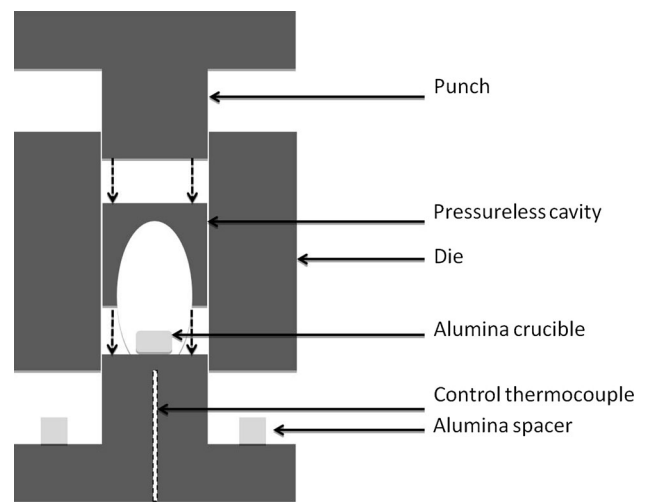


Fig. 1—Assembly used for pressureless sintering in the pulsed electric current sintering (PECS) apparatus.

Table II. Chemical Analysis of the AMDRY 1718 Powder

	Al	C	Co	Cr	Fe	Nb	Ni	Mo	Ti	O
Wt Pct	0.43	0.05	0.09	19.11	17.92	5.07	53.07	3.13	0.94	0.02

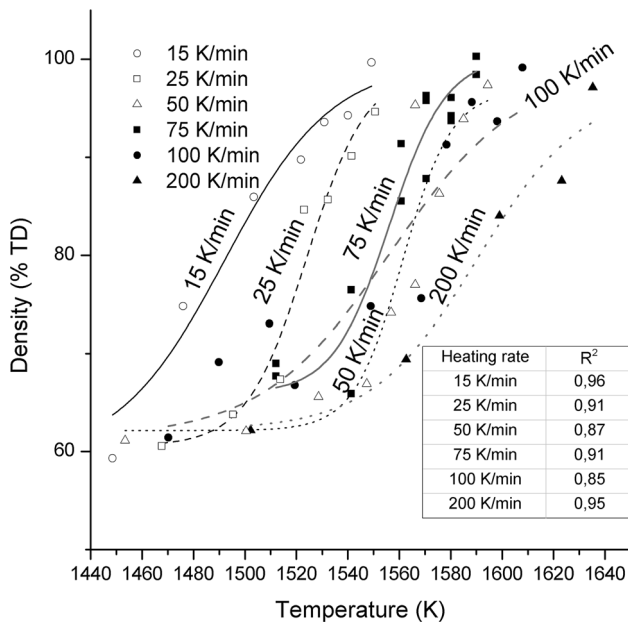


Fig. 2—Sintering data fitted with sigmoidal curves for heating rates of 15, 25, 50, 75, 100, and 200 K/min.

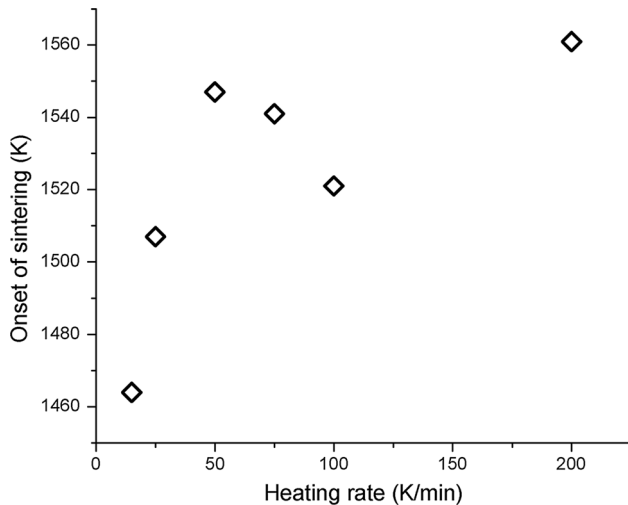


Fig. 3—Onset temperature of densification for each heating rate experiment.

presented, *i.e.*, low (15 to 50 K/minute) and high (75 to 200 K/minute) heating rates.

$$A_2 + \frac{(A_1 - A_2)}{(1 + \exp((x - x_0)/dx))} \quad [5]$$

B. Assessment of Porosity Distribution

Intrinsic heat conduction within the porous compact could create large thermal gradients from the surface to the core when high heating rates are used. Garcia *et al.*^[24] studied the effect of high heating rates during alumina sintering and showed that a thermal gradient between the surface and the material bulk created a

sintering front that was analogous to a solidification front. This phenomenon produced a porosity gradient that is referred to as a “core-shell structure.” This is easily observed as the compact surface approaches full density, while the core remains close to the green density. The Biot number expressed in Eq. [6] was used to evaluate temperature gradients in the compact:

$$Bi = hL/k, \quad [6]$$

where h is the heat transfer coefficient, L is the characteristic length of the body, and k is the thermal conductivity of the body. When the Biot number is larger than 1, a thermal gradient between the surface and the core of the compact exists.

The observed temperature difference between the thermocouple placed in the graphite punch below the sample and the calibrated temperature of the compact is 250 K for a 200 K/minute heating rate. The calculated radiation heat transfer coefficient over the compact surface is used to compute the Biot number for samples with a heating rate of 200 K/minute, assuming a conductivity of 6 W/m/K, and taking into account the initial 40 pct void fraction and the increase of conductivity as the temperature increases.^[25] The Biot number was 0.21 for the sample sintered at 1635 K (1362 °C) for a heating rate of 200 K/minute. The other samples are bound to have smaller Biot numbers since the thermal gradients between the sample and the die walls are lower for the other conditions (*i.e.*, lower heating rates). As the Biot number is less than one, the temperature of the compact can be considered homogeneous during the heating ramp.

The absence of a core-shell structure was experimentally verified by measuring the porosity gradient from the surface to the center of the compact sintered up to 1635 K (1362 °C) at 200 K/minute, as shown in Figure 4. The porosity was between 3.18 and 4.15 pct; however, there was no sign of a porosity gradient.

C. Assessment of Grain Size Evolution

An assumption of the MSC analysis is that grain size is only dependant on density. In most sintering cases, this assumption is largely met. Park *et al.* introduced a grain growth master curve to their MSC analysis to extend the model applications to cases of exaggerated grain growth or substantial surface diffusion.^[26] The validity of this assumption for Inconel 718 was assessed using experimental measurements of the grain size distribution for all sintering conditions used in the study.

The grain size distribution of samples was measured by an image analysis using optical microscopy of etched samples, and a representative micrograph is shown in Figure 5. The average grain size is plotted against density in Figure 6 for each heating rate. The error bars represent the 99 pct confidence interval computed from the grain size distribution for each sample. Two observations can be extracted from this graph. First, the average grain size was not statistically significantly different between the low and high heating rates for all

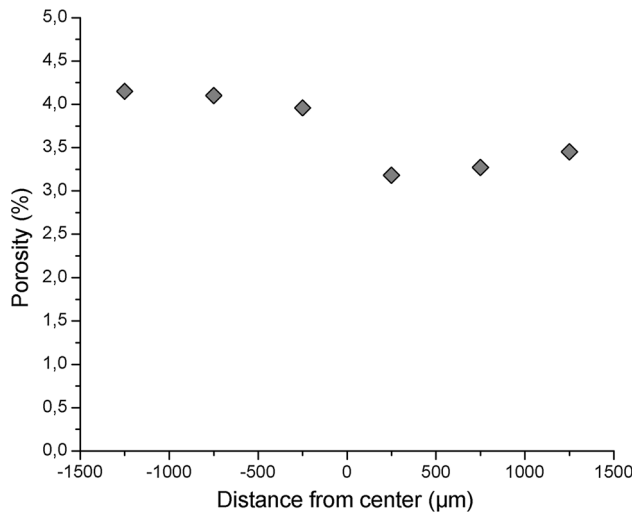


Fig. 4—Porosity measurement across the 200 K/min compact sintered at 1635 K (1362 °C).

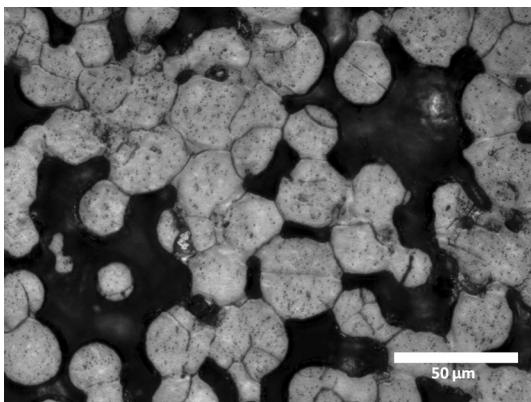


Fig. 5—Micrograph from an etched sample sintered at 1476 K (1203 °C) at 15 K/min.

densities. Second, the average grain size never surpassed the average powder particle size of 33 μm . Accordingly, within the current experimental conditions, the grain size distribution was a function of density only, consistent with the MSC assumption described above.

D. Assessment of Microstructure Evolution

Microstructure observations revealed the formation of a liquid phase during high-temperature excursions, *i.e.*, greater than 1513 K (1240 °C). The micrographs presented in Figure 7 show the liquid phase observed for each heating rate. The liquid fraction was evaluated by image analysis for several samples and these data are presented in Figure 8 with the onset temperature of sintering identified for each heating rate. However, conditions that presented low liquid fractions and low densities could not be analyzed owing to the difficulty of sorting liquation zones from non-wetted grain boundaries. Except for at 75 K/minute, the liquid fraction increased with temperature for all heating rates.

In the samples sintered at over 1540 K (1267 °C), there was a eutectic morphology that can be

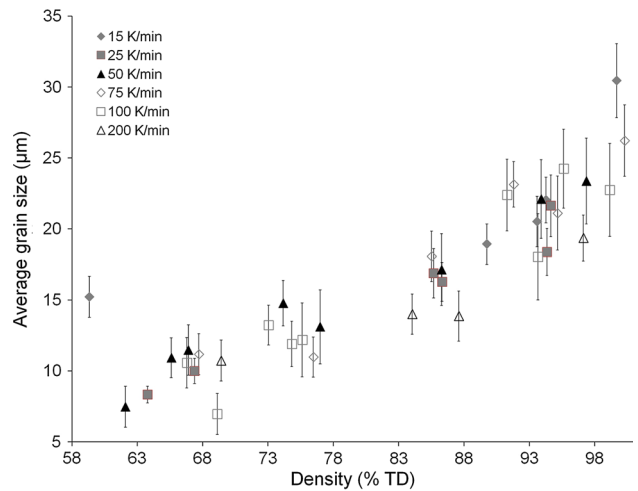


Fig. 6—Average grain size evolution with respect to density plotted for each heating rate used in this study; error bars represent the 99 pct confidence intervals around each value.

distinguished from the surrounding liquation zone. This morphology has been observed by Antonsson and Fredriksson and is associated with the γ /Laves eutectic reaction.^[27] The temperature of the first occurrence of the liquid phase for each heating rate is plotted in Figure 9. The temperature at which liquation was first observed was \sim 1520 K (\sim 1247 °C) for heating rates of 15 and 25 K/minute, 1547 K (1274 °C) for 50 K/minute, \sim 1563 K (\sim 1290 °C) for 75 and 100 K/minute, and 1562 K (1289 °C) for 200 K/minute.

Figure 10 presents the results of an EDS analysis of a γ /Laves eutectic zone in the sample sintered at 200 K/minute and 1635 K (1362 °C). The niobium concentration profile of the matrix, the liquation zone, and the eutectic zone were qualitatively assessed. As expected, the niobium content was higher in the eutectic zone and lower in the liquation zone adjacent to the eutectic region. This observation confirms that the eutectic is a γ /Laves phase.^[27]

E. Determination of Q and MSC Fit

The low and high heating rate sintering curves were analyzed using the MSC methodology described in the Introduction. The data for both solid-state and liquid-state sintering were considered in the analysis to obtain the apparent activation energy of sintering that describes the entire sintering cycle. The onset temperature of sintering (Figure 3) was equal to or higher than the temperature of liquation (Figure 9) for all heating rates, except the lowest one (15 K/minute). The samples sintered at 15 K/minute showed no detectable sign of liquid before 1475 K (1202 °C) (75 pct TD); however, the onset of sintering for this heating rate occurred at 1464 K (1191 °C) (65 pct TD). Since the liquid phase in this sample formed between 1450 K and 1475 K (1177 °C and 1202 °C), it is reasonable to assume that densification largely occurs in the transient liquid-phase regime and that the apparent activation energy is valid if similar liquation conditions are obtained.

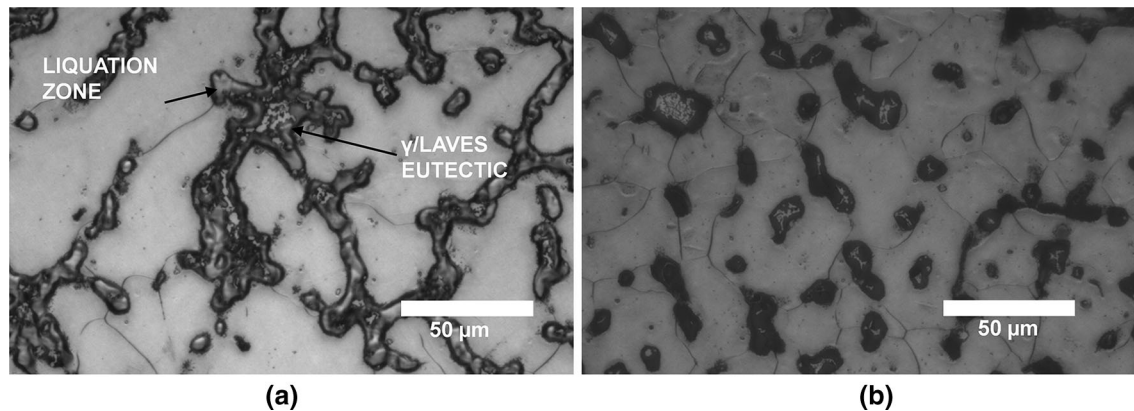


Fig. 7—Optical micrograph of the liquation zone and γ /Laves eutectic for the samples sintered at (a) 15 K/min at 1549 K (1273 °C) and (b) 200 K/min at 1635 K (1362 °C).

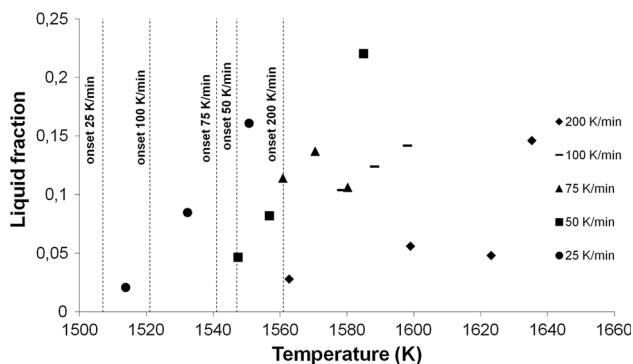


Fig. 8—Measured liquid fractions of several sintered Inconel 718 samples for heating rates from 25 to 200 K/min. The liquid fraction observed is compared with the calculated onset temperature of sintering identified for each heating rate.

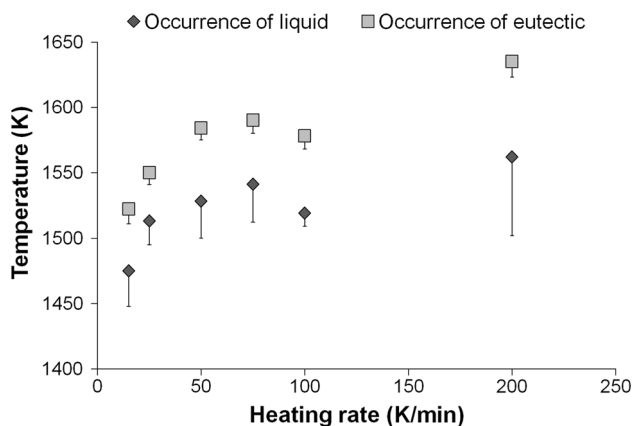


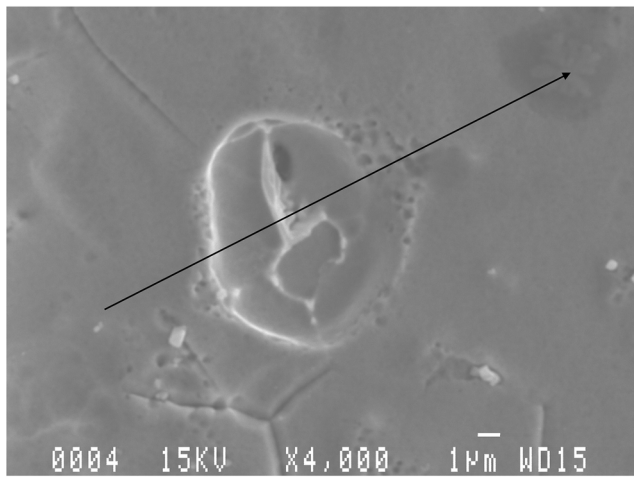
Fig. 9—Temperature of the first observation of liquid-phase and γ /Laves eutectic formation for each heating rate. The error bars indicate the highest temperature sample in which no liquid or eutectic was observed.

The apparent activation energy of sintering was determined by the minimization of residuals between the constructed MSC and the sigmoidal curve fit

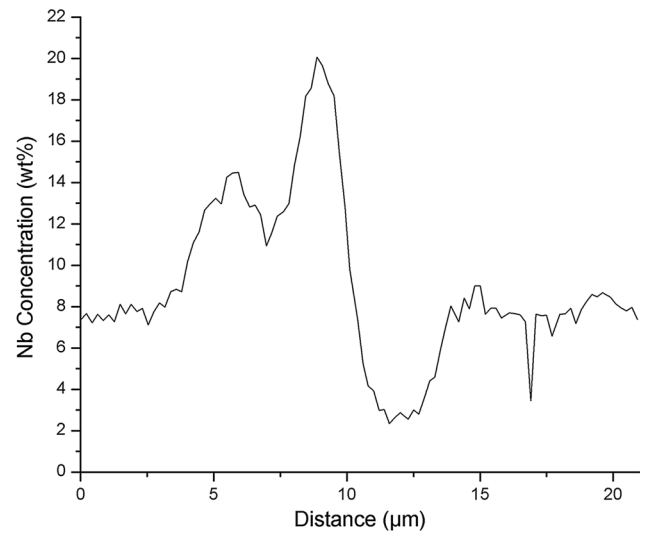
obtained with Eq. [5]. The residuals for the MSC at low and high heating rates were computed for a range of Q and are shown in Figure 11.

The apparent activation energy resulting in the lowest residual for the MSC at the low heating rate was 250 kJ/mol. The apparent activation energy value that minimized the residuals of the MSC for high heating rates was 198 kJ/mol. These activation energies were not significantly different based on a test of variance (F -test) to compare the 95 pct confidence limits for Q . The similarity in activation energy for the low and high heating rates does not however indicate similar MSC behavior, as will be discussed in the next section.

The thermal work integral shown on the right-hand side of Eq. [2] is very sensitive to the apparent activation energy of sintering. Typically, the apparent activation energy of sintering is related to the atomic motion mechanism: surface, boundary, or lattice diffusion. In the case of solid-state sintering, these mechanisms are responsible for material transport from the particles to the pores. Liquid-phase sintering relies on capillary forces, particle sliding, and pore filling to achieve densification.^[28] Liquid-phase sintering behavior is related to the liquid fraction and distribution in the compacted powder (grain size, density, liquid film thickness, and dihedral angle). Thus, the apparent activation energy for liquid-phase sintering should be related to the liquid-state and solid-state diffusion activation energy in proportion to the liquid volume fraction. The diffusion of eutectic forming species and the liquid-state diffusion of nickel should be considered in the apparent activation energy for liquid-phase sintering. The liquid-state diffusion activation energy for nickel is 38 to 42 kJ/mol,^[29,30] and the activation energy for the lattice diffusion of the main alloying elements composing Inconel 718 is given in Table III. Niobium is the main eutectic former, and solid-state diffusion followed by the development of the liquid phase is believed to be the most effective sintering mechanism; accordingly, solid-state diffusion is the limiting factor in the entire sintering cycle, and the activation energy should be close to the corresponding solid-state diffusion energy of Nb in Ni, *i.e.*, 202 kJ/mol.



(a)



(b)

Fig. 10—EDS line scan of the eutectic zone (a), the liquation zone (the arrow shows the region analyzed) (b) line scan Nb profile.

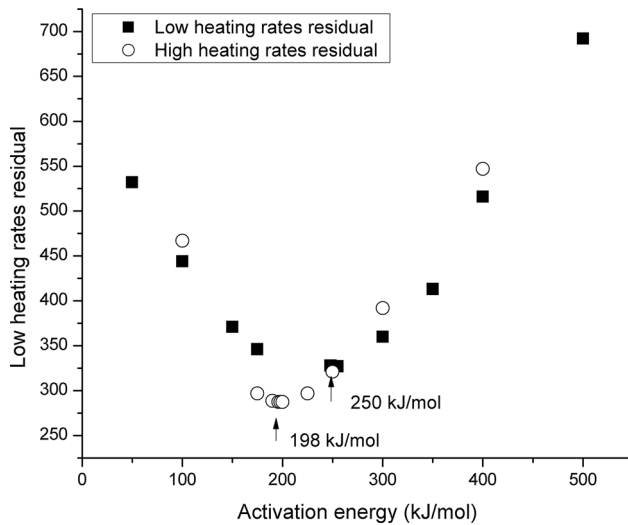


Fig. 11—Residual plot for different values of Q for the low heating rate master sintering curve (MSC) (left) and the high heating rate MSC (right).

Table III. Lattice Diffusion Activation Energy of the Principal Chemical Constituents of Inconel 718 in Nickel

Element	Q (kJ/mol)	References
Ni	285	31
Al	268	32
Ti	257	32
Fe	282	32
Cr	283	33
Nb	202	34

Therefore, the apparent activation energy of sintering observed for high heating rates (198 kJ/mol) was used to compare the MSC for the low and high heating rates shown in Figure 12.

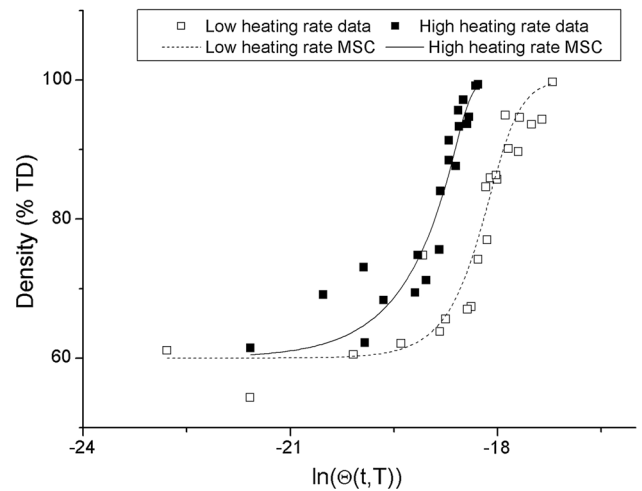


Fig. 12—MSC for Inconel 718 powders sintered in a non-contacting pulsed DC field with an apparent activation energy of 198 kJ/mol for the low and high heating rates.

IV. DISCUSSION

Since the work of Hamjrle *et al.*,^[21,22] it has been suggested that a liquid phase contributes to the sintering of Inconel 718. The liquid phase forms at temperatures between 1435 K and 1485 K (1162 °C and 1212 °C) based on dilatometer measurements performed at 0.23 K/minute.^[21]

The solidification path of Inconel 718 has been described by various authors^[27,35–38]; however, the eutectic reactions and formation temperatures measured during Inconel 718 heating vary markedly among studies, and the temperature ranges are presented in Table IV.

The liquation temperature reported by Hajmrle *et al.*^[21] agrees with the γ /Laves eutectic temperature of 1422 K to 1450 K (1149 °C to 1177 °C). The results presented in Figure 7 confirm that a supersolidus liquid

Table IV. Melting and Solidification Events for Inconel 718

L → γ + Laves	L + NbC → γ + Laves	L → γ + NbC	Solidus	Liquidus
1422 K to 1450 K (1149 °C to 1177 °C)	1433 K (1160 °C)	1498 K to 1594 K (1225 °C to 1321 °C)	1503 K to 1593 K (1230 °C to 1320 °C)	1613 K to 1637 K (1340 °C to 1364 °C)

Table V. Diffusion Depth of Nb at 1498 K (1225 °C) for Heating Rates of 15 to 200 K/min

Heating Rate (K/min)	15	25	50	75	100	200
Diffusion Distance (m)	1.27E-05	9.80E-06	6.92E-06	5.65E-06	4.90E-06	3.47E-06

The diffusion coefficient of Nb in Inconel 718 was set at $0.3 \exp(-35800/T)$, the initial Nb concentration of NbC and the matrix were set at 0.87 and 0.025, respectively Ref. [36].

phase forms during sintering and Figure 9 shows the temperatures at which the liquid phase was first observed. The liquation temperature for the 15 K/minute samples agrees with the results reported by Hajmrlé *et al.*; however, the liquation temperature for heating rates of 25 K/minute and higher increase to ~1503 K to 1563 K (~1230 °C to 1290 °C), while the reported solidus temperature is 1503 K to 1593 K (1230 °C to 1320 °C). The heating rate influences the liquation kinetics; heating rates of less than 15 K/minute promote low-temperature γ/Laves eutectic melting and heating rates of greater than 25 K/minute promote higher melting point events, such as those of the γ/NbC eutectic and solidus.

Liquation is also responsible for the formation of secondary phases (NbC, Laves) at grain boundaries when the sintered compact cools from its processing temperature. The niobium concentration for γ/Laves eutectic formation is 22 pct as compared to 19 pct for γ/NbC eutectic formation. The niobium concentration in Inconel 718 is ~5.5 wt pct. However, its reported partition coefficient of 0.29 to 0.41^[27,35,39] favors segregation. Under the high cooling rate obtained in levitation casting (10^3 to 10^4 K/second), a γ-dendritic structure solidified with ~2 pct Nb in solution, while the interdendritic region contained 16 pct Nb.^[27] Similar cooling rates are obtained in gas atomization, for which it is common to obtain values of 10^3 to 10^6 K/second, depending on particle size.^[40] Assuming that the niobium concentration is similar in the gas-atomized powder structure and the levitation cast samples mentioned above, the γ/Laves eutectic cannot form upon reheating without niobium diffusion from the dendrite core to the interdendritic region. Therefore, upon reheating, Laves phase formation is related to diffusion kinetics and soaking time at the eutectic reaction temperature.

The diffusion distance is proportional to \sqrt{Dt} , where D represents the diffusion coefficient and t is time. Table V shows the results of 1D diffusion calculations, which were performed to evaluate the diffusion distances when the Nb concentration reaches the γ/NbC eutectic composition (19 pct) at the eutectic temperature [(1498 K (1225 °C)].

The Nb diffusion analysis highlights the difference in niobium diffusion depth between the 15 K/minute

(12.7 μm) and 200 K/minute heating rates (3.47 μm). A larger diffusion distance is associated with an increase in the volume of eutectic compound formed at low heating rates. As shown in Figure 9, the temperature of liquid-phase occurrence was ~1475 K (~1202 °C) at heating rates of 15 K/minute and 1513 K to 1563 K (1240 °C to 1290 °C) for rates of 25 to 200 K/minute. Liquation at ~1513 K to 1563 K (1240 °C to 1290 °C) is within the temperature range of both the γ/NbC reaction and solidus but is higher than the γ/Laves eutectic temperature [1422 K to 1450 K (1149 °C to 1177 °C)]. The microstructure did not show the Laves phase until 1522 K, 1550 K, 1584 K, 1590 K, 1578 K, and 1635 K (1249 °C, 1277 °C, 1311 °C, 1317 °C, 1305 °C, and 1362 °C) for heating rates of 15, 25, 50, 75, 100, and 200 K/minute, respectively. This indicates that the niobium concentration did not reach the γ/Laves eutectic composition at the heating rates used in this study and that liquation occurred for a local niobium concentration of less than 22 pct.

The γ/Laves eutectics for samples sintered at 1522 K to 1635 K (1249 °C to 1362 °C) formed during the solidification of the liquid fraction at the relatively slow cooling rate (5 K/second) obtained at the end of the sintering run. The lag between the Laves phase and liquation indicates that a critical liquid fraction is necessary for its formation. Laves phase formation depends on Nb microsegregation during solidification, which is directly related to the solidification velocity, length scale, and solidification time, as shown in Eq. [7]:^[39]

$$MSI \propto \frac{\bar{V} R_f^3}{t_f}, \quad [7]$$

where MSI represents a qualitative microsegregation factor, \bar{V} is the solidification velocity, R_f is the length scale, and t_f is the solidification time. At a very small length scale, microsegregation is negligible, but as the liquid pool increases in radius, microsegregation increases. This could explain the occurrence of the Laves phase only for the samples with the highest temperature for each heating rate studied.

The MSC is used to predict the sintering of powders of the same nature, geometry, and green density with different thermal cycles. For a given thermal cycle, this

model allows the use of a single master curve to calculate the final density of the compact; however, modifications of the underlying sintering mechanism require a different MSC. The sintering of Inconel 718 at heating rates of over 50 K/minute require less thermal work than that at lower heating rates, while the apparent activation energy is similar for all heating rates. A single MSC was not appropriate for the whole range of heating rates studied.

The cause of the observed relationship between heating rate and the densification of Inconel 718 cannot be attributed to thermal gradient or grain size differences, as evidenced by the data presented in Sections III-B and III-C. The physical and geometrical constants used in the MSC model (left-hand side of Eq. [3]) were the same; accordingly, the model cannot explain, in its current state, the effect of heating rate on the sintering of Inconel 718. However, the sintering mechanism is not only solid-state diffusion but also includes the effect of a supersolidus liquid phase. In fact, most sintering occurs in the presence of the liquid phase, as evidenced by the onset temperatures of sintering and the occurrence of liquid. Only the samples sintered at a heating rate of 15 K/minute could possibly include solid-state sintering, when the onset of sintering occurred at 1464 K (1191 °C) and liquation was only observed at 1475 K (1202 °C). The liquid-phase formation kinetics were empirically shown to require less thermal work at heating rates of ≥ 75 than ≤ 50 K/minute. This suggests the addition of a liquid fraction term to the MSC for the analysis of liquid-phase sintering, at least for non-isothermal conditions. The MSC concept was adapted by Bollina *et al.* to analyze the supersolidus liquid-phase sintering of stainless steel 316 with boron addition.^[41] Their analysis involved the fitting of three separate regions of the densification curve with interpolation of the fitting equations between regions to closely match the supersolidus liquid-phase sintering densification data. However, the limited number of densification data points in the present study was not sufficient to use this method. Moreover, the low and high heating rate densification curves were satisfactorily separated with their respective sigmoidal curves.

Since thermal work is the time integral of temperature, the kinetics of liquation can be assessed by comparing the liquid fraction obtained at a given thermal work for low heating rates and high heating rates. Figure 13 presents the measured liquid fraction as a function of the thermal work term from the MSC computed at an apparent activation energy of 198 kJ/mol. The separation of the MSC into two curves (see Figure 12) reflects the difference in liquation kinetics between the 15–50 and 75–200 K/minute rates. The liquid fraction increases with thermal work and the formation of the supersolidus liquid phase typically occurs at lower values of thermal work for high heating rates, as seen by the shift toward lower thermal work for all but one of the high heating rate data points in Figure 13. Thus, the change of trend observed in Figures 2, 3, and 9 is related to the liquation kinetic.

However, additional phenomena linked to the presence of liquid could have contributed to a reduction in

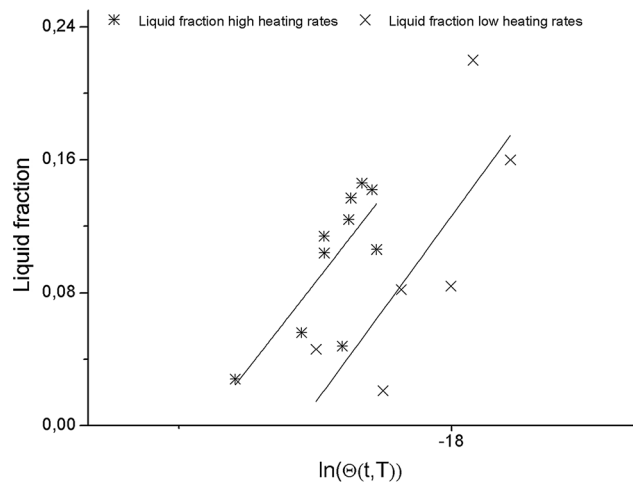


Fig. 13—Liquid fraction as a function of thermal work for low and high heating rates.

the thermal work needed for densification at high heating rates. The diffusion coefficient of Nb in Inconel 718 liquid phase was estimated to be 10^{-9} m²/second compared to 10^{-12} m²/second for solid-state diffusion according to Nastac and Stefanescu.^[39] The liquid phase is a more efficient diffusion phase and will decrease the apparent activation energy of sintering, a phenomenon also observed by Park *et al.*^[19] In addition to the enhanced liquid-phase diffusivity, the capillary force exerted by the liquid at particle boundaries and pore filling also contribute to densification. The observation that an increased sintering heating rate was associated with an increase in the temperature at which liquation occurs indicates that the liquid equilibrium Nb composition and the local Nb distribution at a microscale were functions of heating rate for a given liquid fraction. In turn, this shifted the kinetics of liquid formation toward lower thermal work values at high heating rates. This inclusive liquefaction phenomenon is believed to be the main cause of the MSC shift toward lower thermal work values for heating rates of ≥ 75 than ≤ 50 K/minute.

V. SUMMARY

Sintering of Inconel 718 compacts was studied in a specially designed pressureless pulsed electric current sintering assembly at heating rates ranging from 15 to 200 K/minute. The final density obtained for each heating rate ranged between 94 and 99.7 pct TD. Sintering of Inconel 718 to full density is aided by the formation of a supersolidus liquid phase, as evidenced by the presence of liquid artifacts and the Laves phase during cooling. As such, the sintering behavior could be described by two MSC models that define low (≤ 50 K/minute) and high heating rate (≥ 75 K/minute) behaviors. The apparent activation energy of sintering was statistically similar; a value of 198 kJ/mol, consistent with diffusion data for the species present in Inconel 718, was used for calculations. The difference between the two MSC curves was explained by the difference in liquation kinetics and associated phenomena.

REFERENCES

1. B. Geddes, H. Leon, and X. Huang: ASM International, Materials Park, OH, 2010, pp. xii, 176.
2. G.H. Gessinger: *Powder Metallurgy of Superalloys*, Butterworths, London, 1984.
3. V. Demers, S. Turenne, and O. Scalzo: *J. Mater. Sci.*, 2015, vol. 50 (7), pp. 2893–2902.
4. J.J. Valencia, J. Spirko, and R. Schmees: *Superalloys 718, 625, 706 and Various Derivatives*, 1997, pp. 753–62.
5. H. Wohlfromm, A. Ribbens, J. Maat, M. Blomacher: in *Proceedings Euro PM2003 Congr. Exhib.*, 2003, vol. 3, pp. 207–15.
6. O. Özgün, H.O. Gulsoy, R. Yilmaz, and F. Findik: *J Alloy Compd.*, 2013, vol. 576, pp. 140–53.
7. L. Chang, W. Sun, Y. Cui, F. Zhang, and R. Yang: *J. Alloys Compd.*, 2014, vol. 590, pp. 227–32.
8. A. Guyon, D. Bouvard, J.M. Chaix, and C.P. Carry: *Powder Metall.*, 2014, vol. 57 (1), pp. 54–60.
9. R. Yamanoglu, W. Bradbury, E. Karakulak, E.A. Olevsky, and R.M. German: *Powder Metall.*, 2014, vol. 57 (5), pp. 380–86.
10. P.A. Davies, R. Dunstan, R. Howells, and A.C. Hayward: *Adv. Powder Metall. Part. Mater.*, 2003, vol. 8, pp. 8–12.
11. R. Schmees, J.R. Spirko, and J. Valencia: in *Proceedings of the Advanced Particulate Materials & Processes*, 1997, pp. 493–99.
12. H. Youhua, L. Yimin, H. Hao, L. Jia, and T. Xiao: *Rare Metal. Mat. Eng.*, 2010, vol. 39, pp. 775–80.
13. M.J. Donachie and S.J. Donachie: *Superalloys: A Technical Guide*, 2nd ed., ASM International, Materials Park, OH, 2002.
14. S.A.E. International: AMS 5662M 2009.
15. H.H. Su and D.L. Johnson: *J. Am. Ceram. Soc.*, 1996, vol. 79, pp. 3211–17.
16. J.D. Hansen, R.P. Rusin, M.H. Teng, and D.L. Johnson: *J. Am. Ceram. Soc.*, 1992, vol. 75, pp. 1129–35.
17. M.W. Reiterer and K.G. Ewsuk: *J. Am. Ceram. Soc.*, 2009, vol. 92 (7), pp. 1419–27.
18. K.G. Ewsuk, D.T. Ellerby, and C.B. DiAntonio: *J. Am. Ceram. Soc.*, 2006, vol. 89 (6), pp. 2003–09.
19. S.J. Park, J.M. Martin, J.F. Guo, J.L. Johnson, and R.M. German: *Metall. Mater. Trans. A*, 2006, vol. 37A, pp. 2837–48.
20. J. Wang and R. Raj: *J. Am. Ceram. Soc.*, 1990, vol. 73 (5), pp. 1172–75.
21. K. Hajmrlle and R. Angers: *Int. J. Powder Metall.*, 1980, vol. 16, pp. 255–67.
22. K. Hajmrlle: Forgeage d'ébauches poreuses d'Inconel 718 préparées par coulage en moule poreux et frittage. S.l: Université Laval, 1978. p. xxii, 413 f.
23. W.L. Bradbury and E.A. Olevsky: *Scripta Mater.*, 2010, vol. 63, pp. 77–80.
24. D.E. Garcia, D. Hotza, and R. Janssen: *Int. J. Appl. Ceram. Tech.*, 2011, vol. 8, pp. 1486–93.
25. J.N. Sweet, E.P. Roth, and M. Moss: *Int. J. Thermophys.*, 1987, vol. 8, pp. 593–606.
26. S.J. Park, S.H. Chung, J.M. Martín, J.L. Johnson, and R.M. German: *Metall. Mater. Trans. A*, 2008, vol. 39A, pp. 2941–48.
27. T. Antonsson and H. Fredriksson: *Metall. Mater. Trans. B*, 2005, vol. 36B, pp. 85–96.
28. Z.Z. Fang: *Sintering of Advanced Materials: Fundamentals and Processes*, Woodhead Publishing, Oxford, Philadelphia, 2010.
29. F. Cherne and P. Deymier: *Scripta Mater.*, 1998, vol. 39, pp. 1613–16.
30. P. Protopapas, H.C. Andersen, and N. Parlee: *J. Chem. Phys.*, 1973, vol. 59, pp. 15–25.
31. K. Hirano, R.P. Agarwala, B.L. Averbach, and M. Cohen: *J. Appl. Phys.*, 1962, vol. 33 (10), pp. 3049–54.
32. R.A. Swalin: University Microfilm Publication No. 10043, Ann Arbor, Michigan.
33. S.P. Murarka, R.P. Agarwala, and M.S. Anand: *J. Appl. Phys.*, 1964, vol. 35, pp. 1339–41.
34. R.V. Patil and G.B. Kale: *J. Nucl. Mater.*, 1996, vol. 230, pp. 57–60.
35. G.A. Knorovsky, M.J. Cieslak, T.J. Headley, A.D. Romig, and W.F. Hammett: *Metall. Trans. A*, 1989, vol. 20A, pp. 2149–58.
36. X. Luo, S. Yoshihara, K. Shinozaki, and M. Shirai: *Weld. Res. Abroad*, 2002, vol. 48, pp. 16–24.
37. Y.C. Fayman: *Mater. Sci. Eng.*, 1987, vol. 92, pp. 159–71.
38. W.D. Cao, R.L. Kennedy, and M.P. Willis: *Superalloys 718, 625 and Various Derivatives*, TMS, Warrendale, PA, 1991, pp. 147–60.
39. L. Nastac and D.M. Stefanescu: *Metall. Mater. Trans. A*, 1996, vol. 27A, pp. 4075–83.
40. F. Duflos and J.F. Stohr: *J. Mater. Sci.*, 1982, vol. 17, pp. 3641–52.
41. R. Bollina, S.J. Park, and R.M. German: *Powder Metall.*, 2010, vol. 53, pp. 20–26.